Studies on Incorporation of Mg in Zr-Based AB$_2$ Metal Hydride Alloys

Shiuan Chang [1], Kwo-hsiung Young [2,3,*], Taiehi Ouchi [3], Tiejun Meng [3], Jean Nei [3] and Xin Wu [1]

[1] Department of Mechanical Engineering, Wayne State University, Detroit, MI 48202, USA; shiuanc@wayne.edu (S.C.); xwu@eng.wayne.edu (X.W.)
[2] Department of Chemical Engineering and Materials Science, Wayne State University, Detroit, MI 48202, USA
[3] BASF/Battery Materials-Ovonic, 2983 Waterview Drive, Rochester Hills, MI 48309, USA; taihei.ouchi@basf.com (T.O.); tiejun.meng@partners.basf.com (T.M.); jean.nei@basf.com (J.N.)
[*] Correspondence: kwo.young@basf.com; Tel.: +1-248-293-7000

Abstract: Mg, the A-site atom in C14 (MgZn$_2$), C15 (MgCu$_2$), and C36 (MgNi$_2$) Laves phase alloys, was added to the Zr-based AB$_2$ metal hydride (MH) alloy during induction melting. Due to the high melting temperature of the host alloy (>1500 °C) and high volatility of Mg in the melt, the Mg content of the final ingot is limited to 0.8 at%. A new Mg-rich cubic phase was found in the Mg-containing alloys with a small phase abundance, which contributes to a significant increase in hydrogen storage capacities, the degree of disorder (DOD) in the hydride, the high-rate dischargeability (HRD), and the charge-transfer resistances at both room temperature (RT) and −40 °C. This phase also facilitates the activation process in measurement of electrochemical discharge capacity. Moreover, through a correlation study, the Ni content was found to be detrimental to the storage capacities, while Ti content was found to be more influential in HRD and charge-transfer resistance in this group of AB$_2$ metal hydride (MH) alloys.

Keywords: metal hydride (MH); nickel/metal hydride (Ni/MH) battery; Laves phase alloy; Mg addition; electrochemistry; pressure concentration isotherm

1. Introduction

Laves phase-based AB$_2$ metal hydride (MH) alloy is one of the high-capacity negative electrode materials used in nickel/metal hydride (Ni/MH) batteries. Its reversible hydrogen storage capacity can be as high as 3 wt% [1], which is equivalent to an electrochemical capacity of 804 mAh·g^{-1}. The measured electrochemical discharge capacity can reach up to 436 mAh·g^{-1} [2], which is about 25% higher than the conventional AB$_5$ MH alloys based on rare earth metals (330 mAh·g^{-1}) [3,4]. Early in their development, AB$_2$ MH alloys suffered from a harder activation and a shorter cycle life when compared to AB$_5$ MH alloys [5–8]. With composition and process refinement, the activation and cycle stability of AB$_2$ MH alloys as negative electrode active material improved substantially [9]. However, the high-rate dischargeability (HRD) of the AB$_2$ MH alloys, especially at low temperature, is still significantly inferior to the AB$_5$ MH alloys because of the relatively low nickel content in the AB$_2$ alloy [10]. Various additions, including transition metals—Al [11], Cr [12], Co [13], Cu [14,15], Fe [16], Mo [17,18], Zn [19], Pt [20], Pd [21,22], rare earth metals—Y [23], Ce [24], La [25,26], and Nd [27], and others such as Si [28] and B [29], have been used to reduce the surface charge transfer resistance and increase the HRD of AB$_2$ MH alloys. In this paper, we summarize our findings regarding the use of one of the alkaline earth elements, Mg, as an additive in AB$_2$ MH alloys.

Mg can form various Laves phase alloys with different transition metals, such as C14 (MgZn$_2$), C15 (MgCu$_2$), and C36 (MgNi$_2$) [30]. Mg-containing Mg$_2$Ni, with an hP18 hexagonal structure (derivative

of AlB_2 type [31]), is an important MH alloy that typically works in a temperature range of 200–250 °C. When the crystalline size decreases to the nanoscale or an amorphous state, Mg_2Ni can be used as the negative electrode material in Ni/MH batteries [32–41]. A more suitable stoichiometry for the Mg-Ni system is MgNi (1:1) but, unfortunately, it is not possible to obtain this material through conventional melt-and-cast, according to the phase diagram [42]. Amorphous MgNi prepared by a combination of melt-spin and mechanical alloying can achieve an electrochemical capacity of 720 mAh·g^{-1} for the first cycle. However, it has very poor cycle stability [43] and is, therefore, the subject of a DoE-funded project [44,45]. Reports of Mg use as a modifier in adjusting the hydrogen storage properties of AB_2 MH alloys are very scarce [46], which is very different from Mg-containing superlattice-based MH alloys (reviewed in [47]). Although Mg alone can form Laves phases, Mg is only slightly solubility in Zr(Ti)-based AB_2 phases (0.3 at%) and segregates into a Mg_2Ni phase [46]. The Mg_2Ni secondary phase reduces the surface reaction current, but increases the charge retention [46]. In addition to adding Mg to AB_2 alloy, we also investigated the role of Mg-addition (9.5 at%) in Zr_8Ni_{21} and found that the Mg-added alloy segregates into Zr_7Ni_{10} matrix, consisting of Zr_2Ni_7 grains with occasional Mg_2Ni inclusions, and Mg has a solubility of about 1.5 at% in the Zr_2Ni_7 phase [48]. Additionally, Mg added in Zr_8NNi_{21} alloy hindered the formation process, but increased the surface reaction exchange current [49].

2. Experimental Setup

An induction melting process involving an $MgAl_2O_4$ crucible, an alumina tundish, a 2-kg furnace under argon atmosphere, and a pancake-shaped steel mold was used to prepare the ingot samples. $MgNi_2$ alloy was used as the Mg source, which was added in the final melting step. A 50% excess of Mg was added to compensate for evaporation loss. The ingots were first hydrided/dehydrided to increase their brittleness and then crushed and ground into −200 mesh powder. The chemical compositions of the ingots were analyzed using a Varian Liberty 100 inductively coupled plasma-optical emission spectrometer (ICP-OES, Agilent Technologies, Santa Clara, CA, USA). A Philips X'Pert Pro X-ray diffractometer (XRD, Amsterdam, The Netherlands) was used to study the phase component. A JEOL-JSM6320F scanning electron microscope (SEM, Tokyo, Japan) with energy dispersive spectroscopy (EDS) was applied in investigating the phase distribution and composition. The hydrogen storage was measured using a Suzuki-Shokan multi-channel pressure-concentration-temperature system (PCT, Tokyo, Japan). In PCT analysis, each sample was first activated by a 2-h thermal cycle between room temperature (RT) and 300 °C under 2.5 MPa H_2 pressure, and then measured at 30, 60, and 90 °C. Details of the electrode and cell preparations, as well as the measurement methods, were previously reported [50,51]. AC impedance measurements were conducted using a Solartron 1250 Frequency Response Analyzer (Solartron Analytical, Leicester, UK) with a sine wave amplitude of 10 mV and frequency range of 0.5 mHz to 10 kHz. Prior to experiments, electrodes were subjected to one full charge/discharge cycle at a rate of 0.1C, using a Solartron 1470 Cell Test galvanostat, discharged to 80% state-of-charge, and then cooled to −40 °C. Magnetic susceptibility was measured using a Digital Measurement Systems Model 880 vibrating sample magnetometer (MicroSense, Lowell, MA, USA).

3. Results and Discussion

Six alloys were prepared by the induction melting technique. The design composition, with the ICP results, is summarized in Table 1. The Mg-free base alloy, Mg0, has been used numerous times in the previous comparison works [15–19]. In the design, Mg-content was varied from 0 to 5 at% in alloys Mg0–Mg5, respectively. However, due to the strong rejection from the major phase, the Mg-content in the final alloys is in the range of only 0.6–0.8 at%. To compensate for the increase in Mg-content in the design, both the Ti- and Ni contents were reduced. While the reduction in Ti content is clearly observed in ICP results, the reduction in Ni content is not obvious in alloys Mg1–Mg3, and the average Ni content actually increases in alloys Mg4 and Mg5 because of Mg loss. The average

electron density (*e*/*a*), a strong factor in determining the C14/C15 phase abundance ratio [30,52], decreases monotonically in the design, but stabilized in the beginning and then increases in the ICP results, mirroring the evolution of Ni content. The B/A ratio, defined by the ratio of atomic percentage of B-sites (elements other than Zr, Ti, and Mg) and A-site atoms (Ti, Zr, and Mg), decreases in the design (hypo-stoichiometry), but stabilizes and then increases (hyper-stoichiometry) in the ICP results due to the increase in Ni content. The impact of stoichiometry on the performance of AB_2 MH alloys has been previously studied [53,54]. In general, hypo-stoichiometry promotes the C14 phase, lowers the PCT plateau pressure, and decreases HRD.

Table 1. Design compositions and inductively coupled plasma (ICP) results in at%. *e*/*a* is the average electron density. B/A is the atomic ratio of B-atom (elements other than Ti, Zr, and Mg) to A-atom (Ti, Zr, and Mg).

Alloy	Source	Zr	Ti	V	Cr	Mn	Co	Ni	Mg	Sn	Al	*e*/*a*	B/A
Mg0	Design	21.5	12.0	10.0	7.5	8.1	8.0	32.2	0.0	0.3	0.4	6.82	1.99
	ICP	21.5	12.0	10.0	7.5	8.1	8.0	32.2	0.0	0.4	0.3	6.82	1.99
Mg1	Design	21.5	11.4	10.0	7.5	8.1	8.0	31.8	1.0	0.3	0.4	6.78	1.95
	ICP	21.0	11.3	10.0	7.5	8.3	8.1	32.2	0.6	0.3	0.7	6.82	2.04
Mg2	Design	21.5	10.8	10.0	7.5	8.1	8.0	31.4	2.0	0.3	0.4	6.73	1.92
	ICP	22.5	10.9	9.9	7.2	8.2	8.0	31.8	0.8	0.3	0.4	6.78	1.92
Mg3	Design	21.5	10.2	10.0	7.5	8.1	8.0	31.0	3.0	0.3	0.4	6.69	1.88
	ICP	21.5	10.5	10.3	7.3	8.4	8.4	32.0	0.7	0.3	0.6	6.82	2.06
Mg4	Design	21.5	9.6	10.0	7.5	8.1	8.0	30.6	4.0	0.3	0.4	6.65	1.85
	ICP	21.0	9.6	9.8	6.9	8.3	8.2	34.7	0.6	0.3	0.6	6.96	2.21
Mg5	Design	21.5	9.0	10.0	7.5	8.1	8.0	30.2	5.0	0.3	0.4	6.60	1.82
	ICP	20.5	8.6	9.6	7.0	8.0	7.9	36.7	0.8	0.3	0.6	7.05	2.34

3.1. X-Ray Diffractometer Analysis

XRD analysis is an important tool to study the multi-phase nature of the Laves phase MH alloys [55–58]. The XRD patterns for alloys Mg0–Mg5 are shown in Figure 1. Peaks from the C15 cubic phase overlap with some of those from the C14 hexagonal phase. The TiNi phase with a B2 cubic structure can be seen in most of the XRD patterns. In addition to the C14, C15, and TiNi phases, one more cubic phase was observed in the Mg-containing alloys and it is believed to relate to Mg addition in the alloy. As the alloy number increases (Mg0 → Mg5), the intensities of C14-only peaks (for example, the one near 39.5°) decrease and the main C14/C15 peak (around 42.8°) first shifts to the left (larger unit cell) and then shifts to the right (smaller unit cell), as indicated by the blue vertical line in Figure 1.
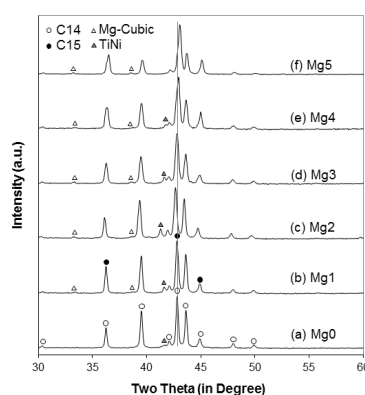

Figure 1. X-ray diffractometer (XRD) patterns using Cu-K*α* as the radiation source for alloys: (**a**) Mg0; (**b**) Mg1; (**c**) Mg2; (**d**) Mg3; (**e**) Mg4; and (**f**) Mg5. In addition to two Laves phases, two cubic phases can be also identified. The vertical line indicates the main C14/C15 peak shifting to lower and then higher angles with an increasing alloy number.

The lattice constants of the four phases obtained from the XRD analysis are listed in Table 2 with the crystallite size of the main C14 phase. With the increase in alloy number, the lattice constants of the C14 phase first increase and then decrease. The changes are very isotropic, as seen from the nearly unchanged a/c ratio. The crystallite size of the C14 phase decreases, and the lattice constants of C15 and TiNi follow the same trend as observed in the C14 main phase.

Table 2. Lattice constants a and c, a/c ratio, unit cell volume, and crystallite size of the main C14 phase of alloys Mg0–Mg5 from XRD analysis. ND denotes non-detectable.

Alloy	Mg0	Mg1	Mg2	Mg3	Mg4	Mg5
C14 a (Å)	4.9545	4.9566	4.9727	4.9593	4.9555	4.9473
C14 c (Å)	8.0733	8.0781	8.1082	8.0846	8.0738	8.0586
C14 a/c	0.6137	0.6136	0.6133	0.6134	0.6138	0.6139
C14 unit cell volume (Å^3)	171.63	171.87	173.64	172.20	171.71	170.82
C14 crystallite size (Å)	685	518	400	385	398	373
C15 a (Å)	6.9932	6.9894	7.0098	6.9926	6.9770	6.9628
TiNi a (Å)	3.0667	3.0674	3.0914	3.0687	3.0590	ND
Mg-related cubic a (Å)	ND	4.6553	4.6655	4.6670	4.6567	4.6711

The phase abundances of four constituent phases, obtained from a Rietveld refinement of the XRD patterns, are listed in Table 3. In general, as the alloy number increases, the C14 phase was replaced by the C15 phase and the TiNi phase abundance first increases and then decreases while the phase abundance of the Mg-related cubic phase remains unchanged. The evolution of the C14/C15 phase agrees with the changes in e/a and B/A (Table 1), because the C14/C15 phase determination threshold of e/a is approximately 6.9 in this case [52].

Table 3. Phase abundances of alloys Mg0–Mg5 from XRD analysis. ND denotes non-detectable.

Alloy	C14 Abundance (%)	C15 Abundance (%)	TiNi Abundance (%)	Cubic Abundance (%)
Mg0	93.7	5.2	1.2	ND
Mg1	81.8	15.9	2.0	0.3
Mg2	88.3	7.9	3.5	0.3
Mg3	72.0	25.1	2.4	0.5
Mg4	56.5	42.2	1.0	0.4
Mg5	36.9	62.6	ND	0.5

3.2. Scanning Electron Microscope/Energy Dispersive Spectroscopy Analysis

SEM back-scattering electron images (BEI) for alloys Mg1–Mg5 are shown in Figure 2. EDS was used to study composition information of representative spots with different contrasts on the BEI micrographs and the results are summarized in Table 4. As we know, EDS is a semi-quantitative analysis and results are only for comparison purpose. The microstructure of the Mg-free alloy (Mg0) was published before (as alloy Mo0 in [17]) and is composed of C14 and TiNi phases. In the microstructures of Mg-containing alloys, a C15 phase (judging from its relatively higher e/a value) with a slightly brighter contrast and an Mg-predominated phase with a darker contrast start to appear. The TiNi phase is usually surrounded by the C15 phase, since the cooling sequence is C14-C15-TiNi [59,60]. According to the EDS results shown in Table 4, the Mg-content in the C14 phase is very small (0.2–0.3 at%), while that of the C15 phase is slightly higher (0.3–0.7 at%). In addition, the B/A ratios in the C14 phase are higher than those in the C15 phases. The initial increase followed by a decrease in the C14 lattice parameters found through XRD analysis can be explained by the balance between the decrease in the content of relatively small Ti (larger C14 unit cell) and the increase in B/A ratio (smaller C14 unit cell [61]). The B/A ratio in the TiNi phase is calculated based on the assumption of V occupying the A-site [27] and the results are still higher than 1, which indicates the possibility of other Zr_xNi_y secondary phases with higher B/A ratios. The nature of the Zr_xNi_y phase

was studied before by transmission electron microscopy [62]. The Mg-rich phase (the fourth phase in each BEI micrograph) has an Mg-content from 45.4 at% to 82.1 at%. It is difficult to link this phase to the cubic phase found by XRD since all alloys in Mg-Ni phase diagram are hexagonal (Mg, Mg_2Ni, and $MgNi_2$). An $MgIn_2$ intermetallic alloy with a cubic structure and a lattice constant of 4.60 Å [63] was the prototype used in our XRD analysis. The phase with the bright contrast (the fifth phase in each BEI micrograph) has a relatively higher Zr-content and a B/A ratio close to 1.0, and therefore is identified as the ZrNi phase. It cannot be the mixture of Zr metal and neighboring Laves phase because of a relatively low V-content (similar to the case of TiNi phase). The corresponding XRD peak of this ZrNi phase cannot be identified due to low abundance. The Mg-contents in the TiNi and ZrNi phases are slightly higher than those in the C14 and C15 phases.
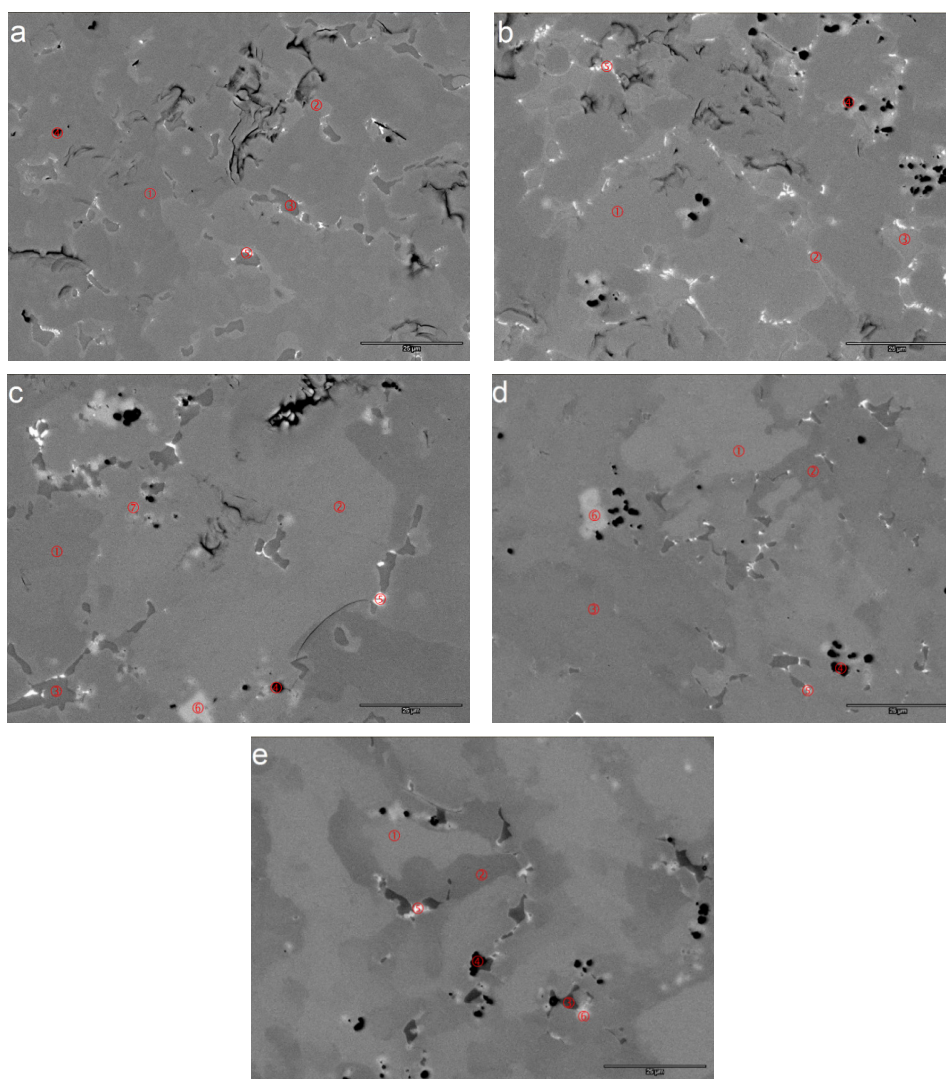

Figure 2. Scanning electron microscope (SEM) back-scattering electron image (BEI) micrographs from alloys: (**a**) Mg1; (**b**) Mg2; (**c**) Mg3; (**d**) Mg4; and (**e**) Mg5. The scale bar at the lower right corner represent 25 μm. The compositions of the numbered areas were analyzed by energy dispersive spectroscopy (EDS), and results are shown in Table 4. Areas 1, 2, 3, 4, 5, and 6 are identified as C14, C15, TiNi, Mg-cubic, ZrNi, and Zr phases, respectively.

Table 4. Summary of EDS results. All compositions are in at%. Compositions of the main C14 and C15 phase are in **bold** and *italic*, respectively.

Area	Zr	Ti	V	Cr	Mn	Co	Ni	Mg	Sn	Al	*e/a*	B/A	Phase
Mg1-1	**20.4**	**10.5**	**11.1**	**8.6**	**8.8**	**8.7**	**31.0**	**0.2**	**0.2**	**0.5**	**6.83**	**2.22**	**C14**
Mg1-2	*21.0*	*12.2*	*6.9*	*4.2*	*6.2*	*6.1*	*41.9*	*0.1*	*0.8*	*0.6*	*7.15*	*2.00*	*C15*
Mg1-3	16.9	23.4	2.4	1.3	3.1	5.9	45.2	0.3	1.1	0.4	7.14	1.33	TiNi
Mg1-4	9.9	8.4	4.6	2.7	3.6	3.6	20.0	46.6	0.4	0.2	4.65	0.54	Mg-cubic
Mg1-5	27.5	12.1	2.2	1.0	2.5	3.2	42.0	0.3	8.9	0.3	6.79	1.05	ZrNi
Mg2-1	**21.9**	**9.9**	**11.9**	**8.0**	**9.1**	**8.7**	**29.4**	**0.3**	**0.2**	**0.6**	**6.74**	**2.12**	**C14**
Mg2-2	*22.8*	*11.6*	*6.7*	*3.7*	*6.4*	*6.2*	*40.9*	*0.4*	*0.8*	*0.5*	*7.08*	*1.87*	*C15*
Mg2-3	20.7	21.4	1.4	0.5	2.3	6.0	45.5	1.2	0.5	0.5	7.09	1.24	TiNi
Mg2-4	12.9	5.7	2.0	1.0	2.0	2.3	16.1	57.2	0.7	0.0	4.03	0.32	Mg-cubic
Mg2-5	29.0	11.7	1.8	0.9	2.5	3.4	41.5	0.9	7.7	0.5	6.74	1.03	ZrNi
Mg3-1	**20.6**	**9.8**	**11.9**	**7.4**	**9.3**	**9.1**	**31.0**	**0.3**	**0.2**	**0.4**	**6.85**	**2.26**	**C14**
Mg3-2	*20.4*	*12.2*	*7.2*	*3.2*	*6.5*	*6.3*	*42.5*	*0.5*	*0.7*	*0.5*	*7.18*	*2.02*	*C15*
Mg3-3	15.6	25.7	1.7	0.4	2.6	5.8	45.6	1.3	0.8	0.6	7.10	1.26	TiNi
Mg3-4	9.2	2.7	0.4	0.2	0.5	0.6	4.2	82.1	0.1	0.0	2.66	0.06	Mg-cubic
Mg3-5	30.7	9.4	1.0	0.6	1.9	2.2	41.1	1.1	11.7	0.4	6.63	0.89	ZrNi
Mg3-6	95.2	1.8	0.3	0.2	0.4	0.3	1.7	0.1	0.0	0.0	4.13	0.03	Zr
Mg3-7	78.1	5.4	2.4	1.3	1.9	2.0	8.4	0.2	0.2	0.0	4.70	0.19	ZrO$_2$
Mg4-1	**22.4**	**7.1**	**12.1**	**12.3**	**10.1**	**9.9**	**25.4**	**0.3**	**0.1**	**0.3**	**6.68**	**2.36**	**C14**
Mg4-2	*19.3*	*12.6*	*7.9*	*3.9*	*6.7*	*6.6*	*41.7*	*0.3*	*0.5*	*0.5*	*7.18*	*2.11*	*C15*
Mg4-3	13.8	26.8	2.0	0.6	3.0	5.8	45.8	0.7	1	0.5	7.14	1.31	TiNi
Mg4-4	7.1	8.9	2.0	0.9	2.1	2.6	19.6	56.0	0.6	0.1	4.28	0.39	Mg-cubic
Mg4-5	26.6	11.5	2.7	1.1	3.1	2.8	42.8	0.6	8.4	0.4	6.83	1.12	ZrNi
Mg4-6	95.1	1.6	0.3	0.2	0.3	0.3	1.9	0.2	0.0	0.0	4.14	0.03	Zr
Mg5-1	**21.8**	**6.3**	**11.1**	**11.9**	**9.4**	**9.8**	**28.8**	**0.3**	**0.1**	**0.4**	**6.84**	**2.52**	**C14**
Mg5-2	*17.6*	*11.7*	*8.6*	*4.0*	*7.2*	*6.4*	*42.8*	*0.7*	*0.4*	*0.6*	*7.25*	*2.33*	*C15*
Mg5-3	8.4	28.8	3.3	0.8	3.9	6.1	45.4	1.0	1.2	1.0	7.16	1.41	TiNi
Mg5-4	12.9	8.0	3.0	1.0	2.4	2.2	24.4	45.4	0.6	0.2	4.79	0.51	Mg-cubic
Mg5-5	25.4	13.0	1.8	0.7	2.1	2.1	44.5	0.3	9.9	0.3	6.87	1.06	ZrNi
Mg5-6	83.6	4.8	1.0	0.7	0.8	0.7	7.8	0.2	0.5	0.0	4.55	0.13	Zr

3.3. Pressure-Concentration-Temperature Analysis

PCT measurement has been used extensively in the study of Laves phase MH alloys reacting with hydrogen gas [64–69]. PCT isotherms measured at 30 °C and 60 °C for alloys Mg0–Mg5 are compared in Figure 3. These isotherms lacking noticeable plateaus are commonly observed in highly-disordered AB$_2$ MH alloys. The multi-phase nature in this group of alloys lowers the critical temperature (T_c) when the pressure plateau starts to disappear [70–72]. Some hydrogen storage properties detected from the PCT isotherms are listed in Table 5. Both the maximum and reversible hydrogen storage capacities first increase and then decrease as the alloy number increases. Due to the lack of obvious plateau pressure, the desorption pressure at 0.75 wt% of hydrogen storage capacity was used for comparison between equilibrium pressure and calculation of hysteresis, and heat of hydride formation (ΔH_h) and change in entropy (ΔS_h). In the Mg-containing alloys, the equilibrium pressure first decreases and then increases as the alloy number increases, which complies with the general rule that a higher metal-hydrogen bond strength yields a lower plateau pressure and a higher hydrogen storage capability [50]. The slope factor (SF) indicates the degree of disorder (DOD) in an alloy. SF is defined as the ratio of the storage capacity between 0.01 MPa and 0.5 MPa to the total capacity in the desorption isotherm [2,19,51]. An alloy with a large SF has a flatter plateau and less DOD (less components or less variations among the components). As the alloy number increases, the SF decreases, indicating an increase in alloy homogeneity with addition of Mg. The hysteresis of the PCT isotherm is defined as $\ln(P_a/P_d)$, where P_a and P_d are the absorption and desorption equilibrium pressures, respectively, at 0.75 wt% H-storage. The irreversible energy loss during plastic deformation of the hydride phase in the alloy matrix is a common explanation for PCT hysteresis [73–75], and was linked to the a/c ratio and pulverization rate of the alloy [76]. In this study, the addition of Mg does not significantly change PCT hysteresis and should have no impact on the pulverization rate of alloy during cycling.
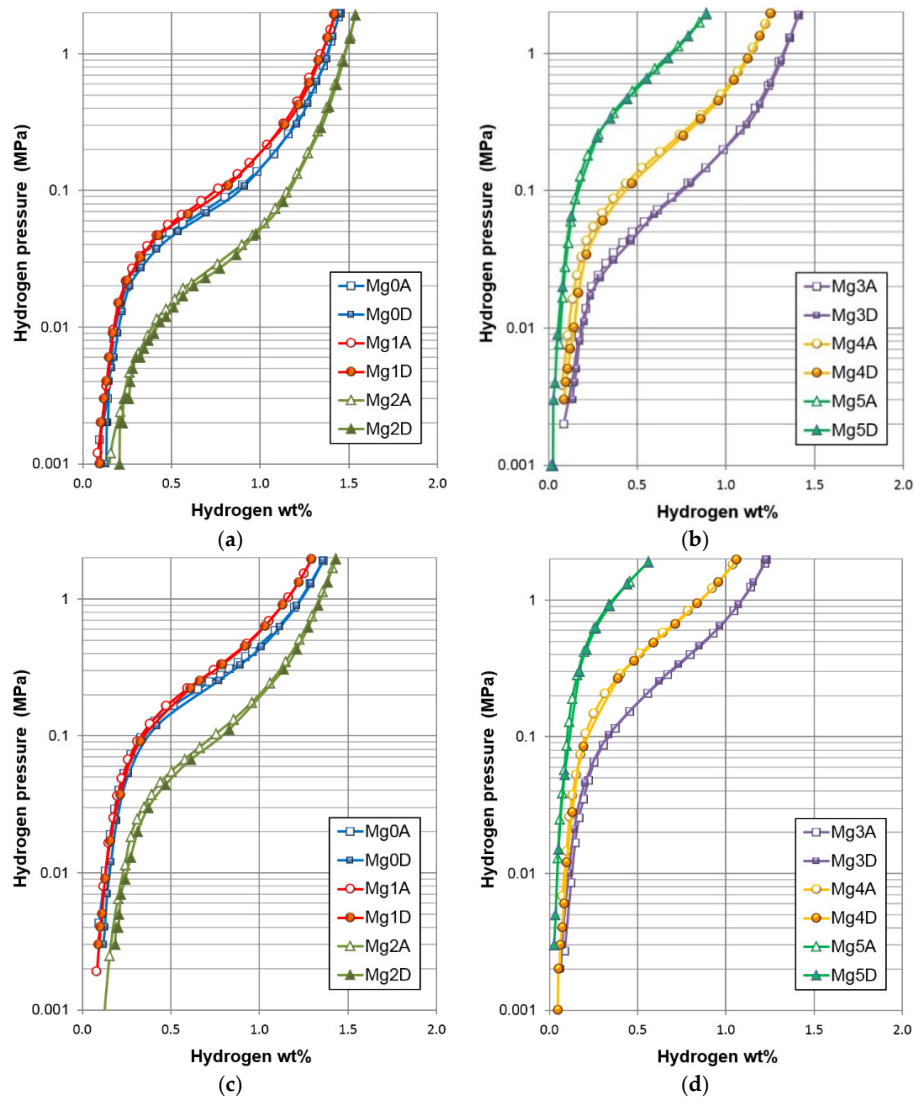
Figure 3. 30 °C pressure-concentration-temperature (PCT) isotherms of alloys: (**a**) Mg0–Mg2 and (**b**) Mg3–Mg5. 60 °C PCT isotherms of alloys: (**c**) Mg0–Mg2 and (**d**) Mg3–Mg5. Open and solid symbols are for absorption and desorption curves, respectively.

Table 5. Summary of the solid state (gaseous phase) hydrogen storage properties of the Mg-containing AB$_2$ alloys. SF: slope factor.

Alloy	Mg0	Mg1	Mg2	Mg3	Mg4	Mg5
Maximum capacity @ 30 °C (wt%)	1.45	1.42	1.54	1.41	1.25	0.89
Reversible capacity @ 30 °C (wt%)	1.32	1.32	1.33	1.30	1.16	0.87
Desorption pressure @ 0.75 wt%, 30 °C (MPa)	0.078	0.096	0.026	0.102	0.246	1.203
SF @ 30 °C	0.60	0.54	0.55	0.51	0.38	0.18
PCT hysteresis @ 0.75 wt%, 30 °C	0.04	0.05	0.10	0.01	0.06	0.02
$-\Delta H_h$ (kJ·mol^{-1})	32.0	32.2	36.2	35.2	31.2	-
$-\Delta S_h$ (J·mol^{-1}·K^{-1})	104	106	108	116	110	-

The desorption equilibrium pressures at the midpoint capacity measured at 30, 60, and 90 °C (*P*) were used to estimate the changes in enthalpy (ΔH_h) and entropy (ΔS_h) using the equation:

$$\Delta G = \Delta H_h - T\Delta S_h = RT\ln P \tag{1}$$

where R is the ideal gas constant and *T* is the absolute temperature. Since the hydrogenation reaction is exothermic, the heat of hydride formation (ΔH_h) is negative. Both ΔH_h and ΔS_h decrease (become more negative) and then increase with the increase in alloy number. The evolution in $-\Delta H_h$ value correlates to hydrogen storage capacity and is agrees with the strength of hydrogen-metal bond assumption described earlier. ΔS_h is an indicator for showing the DOD in hydride from a completely ordered solid (e.g., solid hydrogen). The difference between ΔS_h and -130.7 J·mol^{-1}·K^{-1} (the *S* for H$_2$ (g) at 300 K and 0.1 MPa [77]) can be interpreted as the DOD for hydrogen in the hydride form (β-phase). In this study, the trend of $|\Delta S_h|$ increases, and then decreases with the increase in the alloy number, which is similar to that of SF (the indicator for the DOD in the host metal alloy). The same correlation between the DOD of the hydride and the DOD of the occupied hydrogen was previously reported [19].

3.4. Electrochemical Analysis

Discharge capacities measured at a discharge current of 4 mA·g^{-1} for the first 13 cycles for each alloy in this study are plotted in Figure 4a to show the activation behavior at full capacity. The activation of the Mg-containing alloys appeared to be slightly easier than the Mg-free Mg0 alloy. The results of discharge capacities with other electrochemical tests are listed in Table 6. For Mg-containing alloys, both discharge capacities measured at 4 mA·g^{-1} and 50 mA·g^{-1} rates increase and then decrease with the corresponding increase in the alloy number. The maximum capacities obtained are from alloy Mg2, which demonstrated the lowest *e/a* value and B/A ratio. Mg2 also has the highest hydrogen storage capacity among the alloys in this study. The HRD values, defined as the ratio of the tenth cycle capacities measured at 50 mA·g^{-1} and 4 mA·g^{-1} rates, are listed in Table 6 and demonstrated an increasing trend correlating to alloy number. The HRD obtained from the first 13 cycles are plotted in Figure 4b, which exhibited easier activation in HRD with higher alloy numbers. From Table 6, the addition of Mg is shown to be effective in improving both activation and HRD. The improvement in HRD with Mg was further investigated by electrochemically measuring the bulk diffusion constant (*D*) and surface exchange current (I_o). Method details of these two parameters were previously reported [25] and the results are listed in Table 6. In general, as the alloy number increases, *D* first decreases and then increases while I_o shows the opposite trend. The increase in HRD with alloy number is related to both the bulk and surface properties of the alloys. The addition of Mg decreases the *D* value (bulk), except for alloys with very high Ni content (Mg4 and Mg5), and increases the I_o value (surface) of the alloys. The contribution of Mg to faster activation is similar to that with La in AB$_2$ MH alloys [78–81], where the new Mg-containing phase may absorb a larger amount of hydrogen, causing surface cracking and an increase in the surface area.
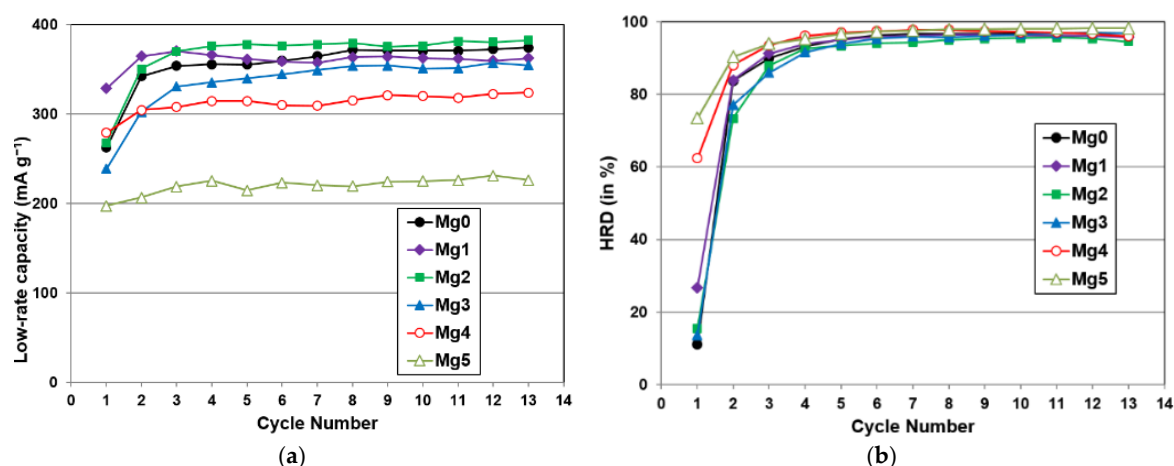

Figure 4. Activation behavior observed from (**a**) half-cell capacity measured at 4 mA·g^{-1} and (**b**) half-cell high-rate dischargeability (HRD) for the first 13 electrochemical cycles.

Table 6. Summary of the room temperature (RT) electrochemical and magnetic results (capacity, rate, D, I_o, and M_s, $H_{1/2}$,) of the Mg-containing AB_2 alloys.

Alloy	Mg0	Mg1	Mg2	Mg3	Mg4	Mg5
10th cycle capacity @ 50 mA·g^{-1} (mAh·g^{-1})	346	327	360	339	311	221
10th cycle capacity @ 4 mA·g^{-1} (mAh·g^{-1})	366	362	377	351	320	225
HRD @ 10th cycle	0.94	0.96	0.96	0.97	0.97	0.98
Number of activation cycles to reach 90% HRD	8	3	4	4	3	2
Diffusion coefficient D (10^{-10} cm^2·s^{-1})	2.5	1.3	1.2	1.8	2.8	2.9
Exchange current I_o (mA·g^{-1})	22.5	31.6	35.8	34.7	27.4	25.9
M_s (emu·g^{-1})	0.0372	0.0388	0.0148	0.0598	0.0730	0.0563
$H_{1/2}$ (kOe)	0.111	0.261	0.260	0.290	0.140	0.118

Low-temperature performance is a very important parameter in propulsion applications, especially in start-stop type micro-hybrid vehicles. The conventional AB_5 MH alloy performed poorly below $-25\,°C$, but the Co-doped A_2B_7 superlattice MH alloy can result in significant improvements [82]. Additions of La, Nd, and Si in AB_2 MH alloys can lower the surface charge-transfer resistance (R) at $-40\,°C$ to a comparable level with AB_5 MH alloys [23,25,27]. In order to study the effect of Mg addition to the low-temperature performance of AB_2 MH alloys, AC impedance at $-40\,°C$ was measured, and R and the double-layer capacitance (C, closely related to the surface reaction area) were calculated from the obtained Cole-Cole plot. R and C values for alloys in this study are listed in Table 7. The addition of Mg into AB_2 MH alloys increases the R value and decreases C. Therefore, different from rare earth elements and Si, the addition of alkaline earth elements in AB_2 MH alloys should not be considered when improvement in the low-temperature performance is needed.

Table 7. Summary of the electrochemical results from AC impedance measurement (R: charge transfer resistance, C: double-layer capacitance at $-40\,°C$ and RT) of the Mg-containing AB_2 alloys.

Alloy	R @ $-40\,°C$ (Ω·g)	C @ $-40\,°C$ (Farad·g^{-1})	R @ RT (Ω·g)	C @ RT (Farad·g^{-1})
Mg0	29	0.24	0.32	0.34
Mg1	38	0.23	0.52	0.45
Mg2	130	0.22	0.56	0.39
Mg3	118	0.21	0.70	0.38
Mg4	90	0.21	0.92	0.30
Mg5	148	0.15	1.44	0.23

3.5. Magnetic Properties

Magnetic susceptibility was used to characterize the nature of the metallic nickel particles present in the surface layer of the alloy following an alkaline activation treatment [10]. Details on the background and experimental methods were reported earlier [83]. Metallic Ni is an active catalyst for the water splitting and recombination reactions that contributes to the I_o in this electrochemical system. This technique allows us to obtain the saturated magnetic susceptibility (M_s), a quantification of the amount of surface metallic Ni (the product of preferential oxidation), and the magnetic field strength at one-half of the M_s value ($H_{1/2}$), a measurement of the averaged reciprocal number of Ni atoms in a metallic cluster (Figure 5a). The magnetic susceptibility graphs for alloys in this study are shown in Figure 5b and the calculated M_s and $H_{1/2}$ values are listed in Table 6. The M_s decreases and then increases with the increase in the alloy number, which is the opposite trend to the data observed for I_o. The increase in I_o for Mg2 is not from the metallic nickel particles embedded in the surface oxide and may be due to the high content of TiNi phase, which was reported as a catalytic phase for electrochemical reaction [84,85]. The $H_{1/2}$ values listed in Table 6 indicate that the size of metallic nickel decreases and then increases as the alloy number increases. In general, the Mg-containing alloys have smaller metallic nickel clusters in the surface than the Mg-free Mg0.
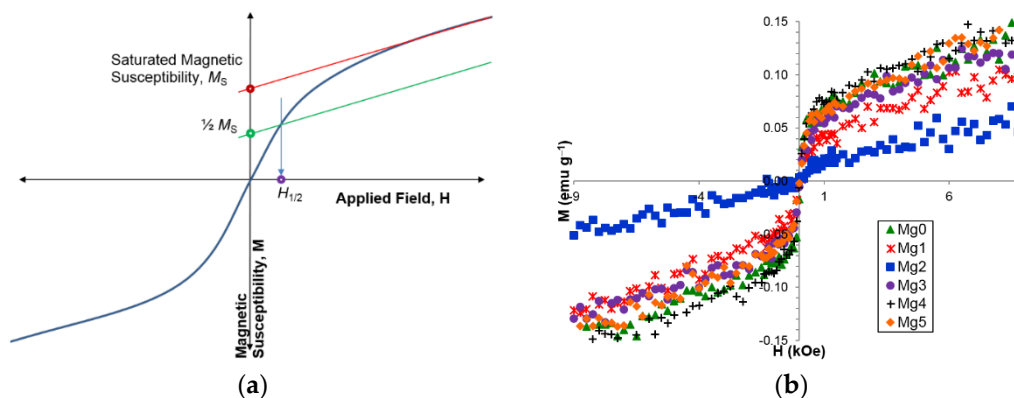
Figure 5. (**a**) Representative magnetic susceptibility measurement results showing the saturated magnetic susceptibility (M_s) with paramagnetic component removed and $H_{1/2}$ defined as the magnitude of applied field corresponding to half of maximum magnetic susceptibility (1/2 M_s); (**b**) the magnetic susceptibility of the alloys in this study.

3.6. Correlations

Due to the limited solubility of Mg in AB$_2$ MH alloys, the ICP results have some deviations from the original design of $Zr_{21.5}Ti_{21-0.6x}V_{10}Cr_{7.5}Mn_{8.1}Co_8Ni_{32.2-0.4x}Mg_xSn_{0.3}Al_{0.4}$, where $x = 0$, 1, 2, 3, 4, and 5, especially in Mg and Ni contents. As the alloy number increases, Mg content remains at approximately the same level, Ni content remain unchanged and then increases for the last two alloys, Mg4 and Mg5, while the Ti content decreases monotonically. In order to study the influences of different compositions with regard to various alloy properties, the correlation factor (R^2) was calculated between composition (Ni content, Ti content, e/a, and B/A) and properties. The comparison results are listed in Table 8. The findings of the correlation can thus be summarized as demonstrating that Ni content has more influences on the B/A ratio, C14 unit cell volume, hydrogen storage properties, low-rate electrochemical capacity, bulk diffusion, and size of metallic Ni embedded in the surface oxide layer when compared to Ti content.

Table 8. Correlation factors (R^2) between the composition and hydrogen storage properties.

Property	Ni Content	Ti Content	C14 Abundance	TiNi Abundance	B/A	e/a
B/A	0.92	0.79	0.94	0.72	1.00	0.96
C14 unit cell volume	0.51	0.19	0.40	0.91	0.63	0.57
C14 crystallite size	0.17	0.61	0.42	0.00	0.20	0.16
C14 abundance	0.88	0.95	1.00	0.49	0.94	0.90
Maximum capacity	0.94	0.76	0.88	0.71	0.93	0.94
Reversible capacity	0.95	0.80	0.87	0.62	0.87	0.92
Plateau pressure	0.84	0.68	0.75	0.57	0.76	0.80
Low rate capacity	0.93	0.79	0.88	0.64	0.90	0.91
HRD	0.45	0.85	0.76	0.08	0.55	0.46
D	0.61	0.31	0.43	0.80	0.59	0.66
I_o	0.25	0.01	0.05	0.70	0.19	0.26
R @ $-40\,^\circ$C	0.21	0.57	0.37	0.00	0.16	0.18
C @ $-40\,^\circ$C	0.76	0.86	0.84	0.33	0.72	0.72
M_s	0.34	0.36	0.49	0.41	0.56	0.43
$H_{1/2}$	0.44	0.09	0.15	0.69	0.30	0.43

The hydrogen capacities obtained from PCT (converted into electrochemical capacity by 1 wt% = 268 mAh$\cdot$g^{-1}) and half-cell tests are plotted against Ni content in Figure 6a, showing a decrease in capacity with an increase in the Ni content. The Ti content is more closely related to the C14 phase crystallite size, C14 phase abundance, HRD, and R and C measured at $-40\,^\circ$C. The last three characteristics are plotted against Ti content in Figure 6b, showing that as Ti content increases,

the R at $-40\,^{\circ}C$ decreases and C at $-40\,^{\circ}C$ increases. However, the RT HRD decreases. The decrease in R is consistent with the increase in C (reaction surface area), but should decrease the RT HRD. The RT R and C follow the trend of $-40\,^{\circ}C$ R and C (Table 7) and, therefore, the discrepancy is not due to different temperatures and requires further investigation. Both C14 and TiNi phase abundances are correlated to various properties. The results show that the C14 main phase abundance is more influential in hydrogen storage capacities both in solid state and electrochemistry, while the TiNi minor phase abundance has high impacts on D, I_o, $H_{1/2}$, and C14 cell volume. The correlation of TiNi phase abundance to D and I_o are plotted in Figure 6c. High amount in TiNi phase increases the surface reactivity (I_o) but hinders the bulk diffusion of hydrogen (D). While the connections between TiNi phase abundance and $H_{1/2}$ may be true and require future validation, the connection with the C14 cell volume is most likely a coincidence. Both B/A ratio and e/a value are not as influential as other factors in this comparison.

Figure 6. Examples of correlations found in this study showing: (**a**) a high Ni content decreases capacities; (**b**) a higher Ti content decreases the HRD and R, while C increases; and (**c**) a higher TiNi phase abundance increases I_o (surface), but decreases D (bulk).

4. Conclusions

The influence of Mg addition (approximately 0.7 at%) to the structural, solid state, and electrochemical properties of a series of Laves phase based AB_2 MH alloys with different Ti and Ni contents were investigated. In general, addition of Mg does not lower the surface charge-transfer resistance, unlike other non-transitional metals, such as Si, Y, La, and Nd. Interestingly, one of the alloys, Mg2 ($Zr_{22.5}Ti_{10.9}V_{9.9}Cr_{7.5}Mn_{8.2}Co_{8.0}Ni_{31.8}Mg_{0.8}Sn_{0.3}Al_{0.4}$) with a phase distribution of 88.3% C14, 7.9% C15, 3.5% TiNi, and 0.3% of a Mg-rich cubic phase, shows improved hydrogen capacities in both solid state and electrochemistry and a higher surface exchange current, but a lower bulk diffusion coefficient.

Author Contributions: Shiuan Chang designed and conducted XRD, PCT, electrochemical, and MS experiments. Taiehi Ouchi prepared the sample. Kwo-hsiung Young, Tiejun Meng, and Xin Wu analyzed the data and participated in the paper preparation.

Conflicts of Interest: The authors declare no conflict of interest.

Abbreviations

MH	Metal hydride
ICP-OES	Inductively coupled plasma-optical emission spectrometer
XRD	X-ray diffractometer
SEM	Scanning electron microscope
EDS	Energy dispersive spectroscopy
PCT	Pressure-concentration-temperature
e/a	Average electron density
ND	Non-detectable
BEI	Back-scattering electron image
DOD	Degree of disorder
D	Diffusion constant
I_o	Surface exchange current
M_s	Saturated magnetic susceptibility
$H_{1/2}$	Magnetic field strength at one-half of the M_s value
RT	Room temperature

References

1. Jacob, I.; Stern, A.; Moran, A.; Shaltiel, D.; Davidov, D. Hydrogen absorption in $(Zr_xTi_{1-x})B_2$ (B = Cr, Mn) and the phenomenological model for the absorption capacity in pseudo-binary Laves-phase compounds. *J. Less Comm. Met.* **1980**, *73*, 1369–1376. [CrossRef]

2. Young, K.; Ouchi, T.; Koch, J.; Fetcenko, M.A. The role of Mn in C14 Laves phase multi-component alloys for NiMH battery application. *J. Alloys Compd.* **2009**, *477*, 749–758. [CrossRef]

3. Hu, W.; Noréus, D. Rare-earth-based AB_5-type hydrogen storage alloys as hydrogen electrode catalysts in alkaline fuel cells. *J. Alloys Compd.* **2003**, *356*, 734–737. [CrossRef]

4. Zhang, Y.; Wang, G.; Dong, X.; Guo, S.; Ren, J.; Wang, X. Effect of substituting Co with Fe on the cycle stabilities of the as-cast and quenched AB_5-type hydrogen storage alloys. *J. Power Sources* **2005**, *148*, 105–111. [CrossRef]

5. Züttle, A.; Meli, F.; Schlapbach, L. Electrochemical and surface properties of $Zr(V_xNi_{1-x})_2$ alloys as hydrogen absorbing electrodes in alkaline electrolyte. *J. Alloys Compd.* **1994**, *203*, 235–241. [CrossRef]

6. Liu, B.; Jung, J.; Lee, H.; Lee, K.; Lee, J. Improved electrochemical performance of AB_2-type metal hydride electrodes activated by the hot-charging process. *J. Alloys Compd.* **1996**, *245*, 132–141. [CrossRef]

7. Yang, X.G.; Lei, Y.Q.; Shu, K.Y.; Lin, G.F.; Zhang, Q.A.; Zhang, W.K.; Zhang, X.B.; Lu, G.L.; Wang, Q.D. Contribution of rare-earths to activation property of Zr-based hydride electrodes. *J. Alloys Compd.* **1999**, *293–295*, 632–636. [CrossRef]

8. Liu, B.; Li, Z.; Higuchi, E.; Suda, S. Improvement of the electrochemical properties of Zr-based AB_2 alloys by an advanced fluorination technique. *J. Alloys Compd.* **1999**, *293–295*, 702–706. [CrossRef]

9. Young, K.H.; Fetcenko, M.A.; Ovshinsky, S.R.; Ouchi, T.; Reichman, B.; Mays, W.C. Improved surface catalysis of Zr-based Laves phase alloys for NiMH Battery. In *Hydrogen at Surface and Interface*; Jerkiewicz, G., Feliu, J.M., Popov, B.N., Eds.; Electrochemical Society: Pennington, NJ, USA, 2000; pp. 60–71.

10. Young, K.; Huang, B.; Regmi, R.K.; Lawes, G.; Liu, Y. Comparisons of metallic clusters imbedded in the surface of AB_2, AB_5, and A_2B_7 alloys. *J. Alloys Compd.* **2010**, *506*, 831–840. [CrossRef]

11. Xu, Y.-H.; Chen, C.-P.; Wang, X.-L.; Wang, Q.-D. The electrode properties of the $Ti_{1.0}Zr_{0.2}Cr_{0.4}Ni_{0.8}V_{0.8-x}Al_x$ (x = 0.0, 0.02, 0.4 and 0.6) alloys. *Mater. Chem. Phys.* **2003**, *77*, 1–5. [CrossRef]

12. Li, L.; Wang, W.; Fan, X.; Jin, X.; Wang, H.; Lei, Y.; Wang, Q.; Chen, L. Microstructure and electrochemical behavior of Cr-added $V_{2.1}TiNi_{0.4}Zr_{0.06}Cr_{0.152}$ hydrogen storage electrode alloy. *Int. J. Hydrog. Energy* **2007**, *32*, 2434–2438. [CrossRef]

13. Zhu, Y.F.; Pan, H.G.; Wang, G.Y.; Gao, M.X.; Ma, J.X.; Chen, C.P.; Wang, Q.D. Phase structure, crystallography and electrochemical properties of Laves phase compounds $Ti_{0.8}Zr_{0.2}V_{1.6}Mn_{0.8-x}M_xNi_{0.6}$ (M = Fe, Al, Cr, Co). *Int. J. Hydrog. Energy* **2001**, *26*, 807–816. [CrossRef]

14. Züttle, A.; Meli, F.; Schlapbach, L. Effects of electrode compacting additives on the cycle life and high-rate dischargeability of $Zr(V_{0.25}Ni_{0.75})_2$ metal hydride electrodes in alkaline solution. *J. Alloys Compd.* **1994**, *206*, 31–38. [CrossRef]

15. Young, K.; Ouchi, T.; Huang, B.; Reichman, B.; Fetcenko, M.A. Studies of copper as a modifier in $C14$-predominant AB_2 metal hydride alloys. *J. Power Sources* **2012**, *204*, 205–212. [CrossRef]

16. Young, K.; Ouchi, T.; Huang, B.; Reichman, B.; Fetcenko, M.A. The structure, hydrogen storage, and electrochemical properties of Fe-doped $C14$-predominating AB_2 metal hydride alloys. *Int. J. Hydrog. Energy* **2011**, *36*, 12296–12304. [CrossRef]

17. Young, K.; Ouchi, T.; Huang, B.; Reichman, B. Effect of molybdenum content on structural, gaseous storage, and electrochemical properties of $C14$-predominant AB_2 metal hydride alloys. *J. Power Sources* **2011**, *196*, 8815–8821. [CrossRef]

18. Erika, T.; Ricardo, F.; Fabricio, R.; Fernando, Z.; Verónica, D. Electrochemical and metallurgical characterization of $ZrCr_{1-x}NiMo_x$ AB_2 metal hydride alloys. *J. Alloys Compd.* **2015**, *649*, 267–274. [CrossRef]

19. Young, K.; Ouchi, T.; Lin, X.; Reichman, B. Effects of Zn-addition to $C14$ metal hydride alloys and comparisons to Si, Fe, Cu, Y, and Mo-additives. *J. Alloys Compd.* **2016**, *655*, 50–59. [CrossRef]

20. Ruiz, F.C.; Peretti, H.A.; Visintin, A.; Triaca, W.E. A study on $ZrCrNiPt_x$ alloys as negative electrode components for NiMH batteries. *Int. J. Hydrog. Energy* **2011**, *36*, 901–906. [CrossRef]

21. Ruiz, F.C.; Peretti, H.A.; Visintin, A. Electrochemical hydrogen storage in $ZrCrNiPd_x$ alloys. *Int. J. Hydrog. Energy* **2010**, *35*, 5963–5967. [CrossRef]

22. Liu, Y.; Zhang, S.; Li, R.; Gao, M.; Zhong, K.; Miao, H.; Pan, H. Electrochemical performance of the Pd-added Ti-V-based hydrogen storage alloy. *Int. J. Hydrog. Energy* **2008**, *33*, 728–734. [CrossRef]

23. Young, K.; Wong, D.F.; Nei, J.; Reichman, B. Electrochemical properties of hypo-stoichiometric Y-doped AB_2 metal hydride alloys at ultra-low temperature. *J. Alloys Compd.* **2015**, *643*, 17–27. [CrossRef]

24. Qiao, Y.; Zhao, M.; Zhu, X.; Cao, G. Microstructure and some dynamic performances of $Ti_{0.17}Zr_{0.08}V_{0.24}RE_{0.01}Cr_{0.1}Ni_{0.3}$ (RE = Ce, Dy) hydrogen storage electrode alloys. *Int. J. Hydrog. Energy* **2007**, *32*, 3427–3434. [CrossRef]

25. Young, K.; Wong, D.F.; Ouchi, T.; Huang, B.; Reichman, B. Effects of La-addition to the structure, hydrogen storage, and electrochemical properties of $C14$ metal hydride alloys. *Electrochim. Acta* **2015**, *174*, 815–825. [CrossRef]

26. Sun, J.C.; Li, S.; Ji, S.J. The effects of the substitution of Ti and La for Zr in $ZrMn_{0.7}V_{0.2}Co_{0.1}Ni_{1.2}$ hydrogen storage alloys on the phase structure and electrochemical properties. *J. Alloys Compd.* **2007**, *446–447*, 630–634. [CrossRef]

27. Wong, D.F.; Young, K.; Nei, J.; Wang, L.; Ng, K.Y.S. Effects of Nd-addition on the structural, hydrogen storage, and electrochemical properties of $C14$ metal hydride alloys. *J. Alloys Compd.* **2015**, *647*, 507–518. [CrossRef]

28. Young, K.; Ouchi, T.; Huang, B.; Reichman, B.; Blankensip, R. Improvement in $-40\ ^{\circ}C$ electrochemical properties of AB_2 metal hydride alloy by silicon incorporation. *J. Alloys Compd.* **2013**, *575*, 65–72. [CrossRef]

29. Li, S.; Wen, B.; Li, X.; Zhai, J. Structure and electrochemical property of ball-milled $Ti_{0.26}Zr_{0.07}Mn_{0.1}Ni_{0.33}V_{0.24}$ alloy with 3 mass% B. *J. Alloys Compd.* **2016**, *654*, 580–585. [CrossRef]

30. Johnson, R.L.; Hoffmann, R.Z. Structure-bonding relationships in the Laves Phases. *Z. Anorg. Allg. Chem.* **1992**, *616*, 105–120. [CrossRef]

31. Pearson, W.B. *The Crystal Chemistry and Physics of Metals and Alloys*; Wiley & Sons: New York, NY, USA, 1971; pp. 514–515.

32. Chen, C.; Wang, C.; Lee, P.; Lin, C. Hydrogen absorption performance of mechanically alloys $(Mg_2Ni)_{100-x}Ti_x$ powder. *Mater. Trans.* **2007**, *48*, 3170–3175. [CrossRef]

33. Gupta, A.; Shervani, S.; Faisal, M.; Balani, K.; Subramaniam, A. Hydrogen storage in Mg-Mg2Ni-carbon hybrids. *J. Alloys Compd.* **2015**, *601*, 280–288. [CrossRef]

34. Zadorozhnyy, V.Y.; Menjo, M.; Zadogozhnyy, M.Y.; Kaloshkin, S.D.; Louzguine-Luzgin, D.D. Hydrogen sorption properties of nanostructured bulk Mg$_2$Ni intermetallic compound. *J. Alloys Compd.* **2014**, *586*, S400–S404. [CrossRef]

35. Zhang, Y.; Li, C.; Cai, Y.; Hu, F.; Liu, Z.; Guo, S. Highly improved electrochemical hydrogen performances of the Nd-Cu-added Mg$_2$Ni-type alloys by melt spinning. *J. Alloys Compd.* **2014**, *584*, 81–86. [CrossRef]

36. Zhu, Y.; Yang, C.; Zhu, J.; Li, L. Structural and electrochemical hydrogen storage properties of Mg$_2$Ni-based alloys. *J. Alloys Compd.* **2011**, *509*, 5309–5314. [CrossRef]

37. Cui, N.; Luo, J.L.; Chuang, K.T. Nickel-metal hydride (Ni-MH) battery using Mg$_2$Ni-type hydrogen storage alloy. *J. Alloys Compd.* **2000**, *302*, 218–226. [CrossRef]

38. Zhang, Y.; Zhang, G.; Yang, T.; Hou, Z.; Guo, S.; Qi, Y.; Zhao, D. Electrochemical and hydrogen absorption/desorption properties of nanocrystalline Mg$_2$Ni-type alloys prepared by melt spinning. *Rare Metal Mater. Eng.* **2012**, *41*, 2069–2074.

39. Zhang, Y.; Ren, H.; Hou, Z.; Zhang, G.; Li, X.; Wang, X. Investigation on gaseous and electrochemical hydrogen storage kinetics of as-quenched nanocrystalline Mg$_2$Ni-type alloys. *Rare Metal Mater. Eng.* **2012**, *41*, 1516–1521.

40. Zhang, Y.; Li, B.; Ren, H.; Hu, F.; Zhang, G.; Guo, S. Gaseous and electrochemical hydrogen storage kinetics of nanocrystalline Mg$_2$Ni-type alloy prepared by rapid quenching. *J. Alloys Compd.* **2011**, *509*, 5604–5610. [CrossRef]

41. Shao, H.; Li, X. Effect of nanostructure and partial substitution on gas absorption and electrochemical properties in Mg$_2$Ni-based alloys. *J. Alloys Compd.* **2016**, *667*, 191–197. [CrossRef]

42. Massalski, T.B. *Binary Alloy Phase Diagram*, 2nd ed.; ASM International: Materials Park, OH, USA, 1990; pp. 2529–2530.

43. Ovshinsky, S.R.; Fetcenko, M.A. Electrochemical Hydrogen Storage Alloys and Batteries Fabricated from Mg Containing Base Alloys. U.S. Patent 5,506,069, 9 April 1996.

44. Yan, S.; Young, K.; Ng, S. Effects of salt additives to the KOH electrolyte used in Ni/MH batteries. *Batteries* **2015**, *1*, 54–73. [CrossRef]

45. Young, K.; Ng, S.K.Y.; Bendersky, L.A. A technical report of robust affordable next generation energy storage system-BASF program. *Batteries* **2016**, *2*. [CrossRef]

46. Young, K.; Ouchi, T.; Huang, B.; Fetcenko, M.A. Effects of B, Fe, Gd, Mg, and C on the structure, hydrogen storage, and electrochemical properties of vanadium-free AB$_2$ metal hydroxide alloy. *J. Alloys Compd.* **2012**, *511*, 242–250. [CrossRef]

47. Liu, Y.; Cao, Y.; Huang, L.; Gao, M.; Pan, H. Rare earth-Mg-Ni-based hydrogen storage alloys as negative electrode materials for Ni/MH batteries. *J. Alloys Compd.* **2011**, *509*, 675–686. [CrossRef]

48. Nei, J.; Young, K.; Salley, S.O.; Ng, K.Y.S. Effects of annealing on Zr$_8$Ni$_{19}$X$_2$ (*X* = Ni, Mg, Al, Sc, V, Mn, Co, Sn, La, and Hf): Structural characteristics. *J. Alloys Compd.* **2012**, *516*, 144–152. [CrossRef]

49. Nei, J.; Young, K.; Salley, S.O.; Ng, K.Y.S. Effects of annealing on Zr$_8$Ni$_{19}$X$_2$ (*X* = Ni, Mg, Al, Sc, V, Mn, Co, Sn, La, and Hf): Hydrogen storage and electrochemical properties. *Int. J. Hydrog. Energy* **2012**, *37*, 8418–8427. [CrossRef]

50. Young, K.; Fetcenko, M.A.; Li, F.; Ouchi, T. Structural, thermodynamics, and electrochemical properties of Ti$_x$Zr$_{1−x}$(VNiCrMnCoAl)$_2$ C14 Laves phase alloys. *J. Alloys Compd.* **2008**, *464*, 238–247. [CrossRef]

51. Young, K.; Fetcenko, M.A.; Koch, J.; Morii, K.; Shimizu, T. Studies of Sn, Co, Al, and Fe additives in C14/C15 Laves alloys for NiMH battery application by orthogonal arrays. *J. Alloys Compd.* **2009**, *486*, 559–569. [CrossRef]

52. Nei, J.; Young, K.; Salley, S.O.; Ng, K.Y.S. Determination of C14/C15 phase abundance in Laves phase alloys. *Mat. Chem. Phys.* **2012**, *136*, 520–527. [CrossRef]

53. Zhu, Y.; Pan, H.; Gao, M.; Ma, J.; Lei, Y.; Wang, Q. Electrochemical studies on the Ti-Zr-V-Mn-Cr-Ni hydrogen storage electrode alloys. *Int. J. Hydrog. Energy* **2003**, *28*, 311–316. [CrossRef]

54. Pan, H.; Zhu, Y.; Gao, M.; Liu, Y.; Li, R.; Lei, Y.; Wang, Q. A study on the cycling stability of the Ti-V-based hydrogen storage electrode alloys. *J. Alloys Compd.* **2004**, *364*, 271–279. [CrossRef]

55. Chen, L.; Wu, F.; Tong, M.; Chen, D.M.; Long, R.B.; Shang, Z.Q.; Liu, H.; Sun, W.S.; Yang, K.; Wang, L.B.; *et al.* Advanced nanocrystalline Zr-based AB_2 hydrogen storage electrode materials for NiMH EV batteries. *J. Alloys Compd.* **1999**, *293–295*, 508–520. [CrossRef]

56. Li, Z.P.; Higuchi, E.; Liu, B.H.; Suda, S. Electrochemical properties and characteristics of a fluorinated AB_2-alloy. *J. Alloys Compd.* **1999**, *293–295*, 593–600. [CrossRef]

57. Young, K.; Ouchi, T.; Yang, J.; Fetcenko, M.A. Studies of off-stoichiometric AB_2 metal hydride alloy: Part 1. Structural characteristics. *Int. J. Hydrog. Energy* **2011**, *36*, 11137–11145. [CrossRef]

58. Lee, S.M.; Lee, H.; Yu, J.S.; Fateev, G.A.; Lee, J.Y. The activation characteristics of a Zr-based hydrogen storage alloy electrode surface-modified by ball-milling process. *J. Alloys Compd.* **1999**, *292*, 258–265. [CrossRef]

59. Liu, Y.; Young, K. Microstructure investigation on metal hydride alloys by electron backscatter diffraction technique. *Batteries* **2016**. to be submitted for publication.

60. Boettinger, W.J.; Newbury, D.E.; Wang, K.; Bendersky, L.A.; Chiu, C.; Kattner, U.R.; Young, K.; Chao, B. Examination of multiphase $(Zr,Ti)(V,Cr,Mn,Ni)_2$ Ni-MH electrode alloys: Part I. Dendritic solidification structure. *Metal. Mater Trans. A* **2010**, *41*, 2033–2047. [CrossRef]

61. Young, K. Stoichiometry in Inter-Metallic Compounds for Hydrogen Storage Applications. In *Stoichiometry and Materials Science—When Numbers Matter*; Innocenti, A., Kamarulzaman, N., Eds.; Intech: Rijeka, Croatia, 2012; pp. 162–164.

62. Bendersky, L.A.; Wang, K.; Boettinger, W.J.; Newbury, D.E.; Young, K.; Chao, B. Examination of multiphase $(Zr,Ti)(V,Cr,Mn,Ni)_2$ Ni-MH electrode alloys: Part II. Solid-state transformation of the interdendric B_2 phase. *Metal. Mater Trans. A* **2010**, *41*, 1891–1906. [CrossRef]

63. Pearson, W.B. *A Handbook of Lattice Spacings and Structures of Metals and Alloys: International Series of Monographs on Metal Physics and Physical Metallurgy*; Elsevier: Philadelphia, PA, USA, 2013; Volume 4, p. 693.

64. Shaltiel, D.; Jacob, I.; Davidov, D. Hydrogen absorption and desorption properties of AB_2 Laves-phase pseudobinary compounds. *J. Less Common Met.* **1977**, *53*, 117–131. [CrossRef]

65. Jacob, I.; Shaltiel, D. Hydrogen sorption properties of some AB_2 Laves phase compounds. *J. Less Common Met.* **1979**, *65*, 117–128. [CrossRef]

66. Qian, S.; Northwood, D.O. Thermodynamic characterization of $Zr(Fe_xCr_{1-x})$ systems. *J. Less Common Met.* **1989**, *147*, 149–159. [CrossRef]

67. Perevesenzew, A.; Lanzel, E.; Eder, O.J.; Tuscher, E.; Weinzierl, P. Thermodynamics and kinetics of hydrogen absorption in intermetallic compounds $Zr(Cr_{1-x}V_x)_2$. *J. Less Common Met.* **1988**, *143*, 39–47. [CrossRef]

68. Park, J.; Lee, J. Thermodynamic properties of the $Zr_{0.8}Ti_{0.2}(Mn_xCr_{1-x})Fe$ system. *J. Less Common Met.* **1991**, *167*, 245–253.

69. Drašner, A.; Blažina, Ž. On the structural and hydrogen desorption properties of the $Zr(Cr_{1-x}Cu_x)_2$ alloys. *J. Less Common Met.* **1991**, *175*, 103–108. [CrossRef]

70. Schlapbach, L.; Züttel, A. Hydrogen-storage materials for mobile applications. *Nature* **2001**, *414*, 353–358. [CrossRef] [PubMed]

71. Züttel, A. Materials for hydrogen storage. *Mater. Today* **2003**, *6*, 24–33. [CrossRef]

72. Sastri, M.V.C. Introduction to Metal Hydrides: Basic Chemistry and Thermodynamics of Their Formation. In *Metal Hydride*; Sastri, M.V.C., Viswanathan, B., Murthy, S.S., Eds.; Springer-Verlag: Berlin, Germany, 1998; p. 5.

73. Scholtus, N.A.; Hall, W.K. Hysteresis in the palladium-hydrogen system. *J. Chem. Phys.* **1963**, *39*, 868–870. [CrossRef]

74. Makenas, B.J.; Birnbaum, H.K. Phase changes in the niobium-hydrogen system 1: Accommodation effcts during hydrde precipitation. *Acta Metal. Mater.* **1980**, *28*, 979–988. [CrossRef]

75. Balasubramaniam, R. Accommodation effects during room temperature hydrogen transformations in the niobium-hydrogen system. *Acta Metal. Mater.* **1993**, *41*, 3341–3349. [CrossRef]

76. Young, K.; Ouchi, T.; Fetcenko, M.A. Pressure-composition-temperature hysteresis in C14 Laves phase alloys: Part 1. Simple ternary alloys. *J. Alloys Compd.* **2009**, *480*, 428–433. [CrossRef]

77. Lide, D.R. *CRC Handbook of Chemistry and Physics*, 74 ed.; CRC Press: Boca Raton, FL, USA, 1993; pp. 6–22.

78. Kim, S.; Lee, J.; Park, H. A study of the activation behaviour of ZrCrNiLa metal hydride electrodes in alkaline solution. *J. Alloys Compd.* **1994**, *205*, 225–229. [CrossRef]

79. Jung, J.; Lee, K.; Lee, J. The activation mechanism of Zr-based alloy electrodes. *J. Alloys Compd.* **1995**, *226*, 166–169. [CrossRef]

80. Park, H.Y.; Cho, W.I.; Cho, B.W.; Jang, H.; Lee, S.R.; Yun, K.S. Effect of fluorination on the lanthanum-doped AB_2-type metal hydride electrodes. *J. Power Sources* **2001**, *92*, 149–156. [CrossRef]

81. Park, H.Y.; Chang, I.; Cho, W.I.; Cho, B.W.; Jang, H.; Lee, S.R.; Yun, K.S. Electrode characteristics of the Cr and La doped AB_2-type hydrogen storage alloys. *Int. J. Hydrog. Energy* **2001**, *26*, 949–955. [CrossRef]

82. Wang, L.; Young, K.; Meng, T.; English, N.; Yasuoka, S. Partial substitution of cobalt for nickel in mixed area earth metal based superlattice hydrogen absorbing alloy—Part 2 battery performance and failure analysis. *J. Alloys Compd.* **2016**, *664*, 417–427. [CrossRef]

83. Nei, J.; Young, K.; Regmi, R.; Lawes, G.; Salley, S.O.; Ng, K.Y.S. Gaseous phase hydrogen storage and electrochemical properties of Zr_8Ni_{21}, Zr_7Ni_{10}, Zr_9Ni_{11}, and ZrNi metal hydride alloys. *Int. J. Hydrog. Energy* **2012**, *37*, 16042–16055. [CrossRef]

84. Zlatanova, Z.; Spassov, T.; Eggeler, G.; Spassova, M. Synthesis and hydriding/dehydriding properties of Mg_2Ni-AB (AB = TiNi or TiFe) nanocomposites. *Int. J. Hydrog. Energy* **2011**, *36*, 7559–7566. [CrossRef]

85. Balcerzak, M. Electrochemical and structural studies on Ti-Zr-Ni and Ti-Zr-Ni-Pd alloys and composites. *J. Alloys Compd.* **2016**, *658*, 576–587. [CrossRef]